CrossMark

Influence of catalyst layer thickness on the growth of nickel silicide nanowires and its application for Li-ion batteries

Isaac N. Lund [a,b,*], Jae Ho Lee [a,b], Harry Efstathiadis [a], Pradeep Haldar [a], Robert E. Geer [a]

[a] College of Nanoscale Science and Engineering, State University of New York, 255 Fuller Rd, Albany, NY 12203, USA
[b] Battery Energy Storage System — Technologies, 90 S Pine Ave Apt D, Albany, NY 12208, USA

HIGHLIGHTS

- Correlation of nickel silicide nanowire phase and morphology based on amount of free catalyst.
- Creation of a novel heterogeneous $NiSi_2$ crystalline core Ni doped SiO amorphous shell nanowire.
- Displaying high capacity and high retention performance of heterogeneous nanowire when used as an anode for Li-ion battery.
- Displaying surface passivating characteristics during full charging of a Si based anode.

ARTICLE INFO

ABSTRACT

We report the influence of nickel catalyst layer thickness when growing nickel silicide alloy nanowires below the liquefaction temperature through metal induced growth. Three different catalyst layer thicknesses show three different nanowire growth results that vary significantly the performance when used as an anode in a lithium ion solution. The thicker catalyst layers (70 nm) show pure NiSi nanowires which have an initial capacity of 1300 mAh g^{-1} that degrades to 550 mAh g^{-1} within 90 cycles. The thinner (30 nm thick) layer shows a heterogenous nanowire morphology comprising of a multicrystalline $NiSi_2$ inside core and a Ni doped SiO amorphous shell with initial Li-ion capacity of 1727 mAh g^{-1} capacity that increases to 2468 mAh g^{-1} after 90 cycles. Samples with no catalyst layers were shown to grow pure silicon nanowires with poor surface coverage having an initial capacity of 1779 mAh g^{-1} that falls to 242 mAh g^{-1} after 90 cycles.

1. Introduction

Lithium-ion (Li-ion) batteries are the energy storage devices of choice for items ranging from portable electronic devices to electric vehicles (EVs). The desire to improve the overall capacity and thus the battery life between charges has spurred research into higher capacity electrodes. The research into the negative side of the battery (the anode) has mainly focused around the holy grail of anode materials Si. Si has the highest theoretical capacity of 4422 mAh g^{-1} which is 11× higher than the commercially used graphite anode which has a theoretical capacity of 372 mAh g^{-1} [1–5]. While Si has the highest theoretical capacity use of Si as an anode material for Li ion batteries has been plagued by two separate problems. The first is the expansion and contraction that occurs during lithium insertion and extraction which creates internal stresses that can crack and degrade the material over several charges until the material is pulverized [1–4]. This was solved by utilizing Si in nanoscale dimensions and is specifically shown that any Si particles size under 150 nm will not be subjected to pulverization like bulk Si [6]. The second problem with the integration of Si for use as an anode material is the creation of an unstable passivation layer known as a solid electrolyte interphase (SEI) layer [1–5]. This passivation layer is created upon the first several cycles of the Si anode material with the electrolyte and is comprised of the reactive silicon anode and decomposition products in the electrolyte [5,7]. The SEI creates a problem since it traps Li atoms into the decomposition products making those ions unavailable to carry charge, it is created when unpassivated material contacts the electrolyte which for Si occurs throughout the charging cycle due to volume expansion [5,7].

* Corresponding author. College of Nanoscale Science and Engineering, State University of New York, 255 Fuller Rd, Albany, NY 12203, USA. Tel.: +1 831 247 1109; fax: +1 518 437 8603.

E-mail address: ilund@albany.edu (I.N. Lund).

Nickel silicide has been shown to have a high capacitance for Li-ion batteries when it is in its monosilicide (NiSi) phase (1360 mAh g^{-1}) or a lower capacity when in its most stable form nickel disilicide (NiSi$_2$) (562 mAh g^{-1}) phase [8–15]. NiSi has also been shown to separate into pure Ni and Si during alloying with Li as shown in Equation (1) with Ni buffering the expansion of Si to reduce pulverization and conductively doping Si to increase columbic efficiency [8–12,14]. The difference in the reaction to lithium between these two silicide phases has to do with the affinity of Si to remain bonded to Ni or become separated when alloyed [8–12,14]. For NiSi the nickel and silicon separate into Ni and Si upon lithiation with the Si maintaining the same Li capacity as bulk Si, however the overall capacity is degraded by the parasitic weight of Ni [8–12,14]. This interaction has been shown to be reversible but still degrade over multiple cycles without the use of a surface passivating carbon film [9–13]. The use of a surface passivating carbon film is needed in order to isolate the Si surface from the electrolyte to stop the formation and growth of an unstable SEI layer since carbon creates a stable SEI interface [8]. The direct coating of C on top of Si has been attempted with unsuccessful results since the lattice mismatch between C and Si strains the C which is exacerbated when the Si is alloyed with Li to create a 400% volume expansion [8]. Thus any attempt to coat C directly on top of Si to be used as an anode for Li ion battery has shown the C to be exfoliated off and the Si capacity to degrade with SEI formation [8]. The addition of Ni in the Si lattice should buffer the expansion by 200% which during lithiation would still create a 200% strain to the Si–C bond and should exfoliate it from the surface [8,10–12]. Thus the cycling improvements for using C coated NiSi anodes have been unaddressed as known by this author and is assumed to only be relatively short term cycling improvement. Thus the utilization of a Ni–Si alloy has not been shown to be stable for prolonged Li ion battery cycling.

$$5\text{NiSi} + 22\text{Li} \leftrightarrow 5\text{Ni} + \text{Li}_{22}\text{Si}_5: \text{capacity: } 1360 \text{ mAh g}^{-1} \qquad (1)$$
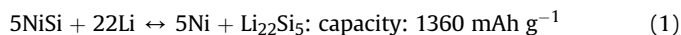
Nickel has been shown to be able to grow nanowires at temperatures below the liquefaction temperature for the nickel catalyst [16,17]. The liquefaction of the catalyst particle is required for standard vapor liquid solid growth in the presence of silane (SiH$_4$) vapor [18]. It has been shown that Ni catalyst can produce preferential one dimension nanowire growth below Ni liquefaction temperatures by metal induced growth [16,17]. Metal induced growth utilizes the property that SiH$_4$ preferentially decomposes into a Ni catalyst and Ni preferentially diffuses up a Si rich Ni$_x$Si$_y$ phase to expose itself to further SiH$_4$ decomposition making the one dimensional growth [16,17]. To understand the influence of Ni availability on the morphology of the growing nanowires and its subsequent performance when used as an anode in Li-ion batteries three different catalyst layer thicknesses were chosen for metal induced silicide nanowire growth: a 70 nm thick Ni layer, a 30 nm thick Ni layer, and no catalyst layer. In this paper we show the effect of catalyst layer thickness on the resulting morphology and phase of the grown nanowires and its effect when utilized on device performance when utilized as an anode for Li-ion batteries.

2. Experimental

2.1. Material preparation and growth

A Ni catalyst layer is deposited onto a 3 mm thick 304 stainless steel substrate in an e-beam evaporator utilizing 99.99% pure Ni pellets. The thickness of the catalyst layer deposited was varied into three thicknesses: no deposition, 30 nm thick, and 70 nm thick

deposited Ni. The thicknesses resulted in 3 different growth regimes which are: no deposition, yielded pure silicon nanowires (SiNW), 30 nm thick yielded heterogenous multicrystalline NiSi$_2$ core and amorphous Ni doped-SiO shell nanowires, and 70 nm thick Ni yielded pure NiSi nanowires.

The growth was performed by the catalytic decomposition of 1% silane with the remainder Ar gas in a horizontal CVD furnace. The samples were placed in the furnace and the furnace was pumped down to vacuum and allowed to sit for 1 h. The growth of the samples occurred at 100 Torr under 100 sccm 1% SiH$_4$ + 99% Ar flow for 1 h at 650 °C. During heating up Ar is flowed through an MFC at 100 sccm into the tube furnace for a period of 30 min followed by a dwell time of 15 min to allow for the furnace temperature to regulate at 650 °C. Once temperature has stabilized pure Ar flow is turned off and 1% SiH$_4$ + 99% Ar while pressure is set. Following the growth step the flow is turned off, the heater is shut off and the throttling valve is opened to place the furnace under vacuum for cool down.

2.2. Material characterization

The morphology, size, and surface coverage of the nanowires is shown in the LEO 1550 SEM with an accelerating voltage of 4 keV and by low resolution JEOL 1550 STEM with an accelerating voltage of 300 keV. The TEM samples were made by sonicating a nanowire sample in an ethyl alcohol solution for a period of 5 min, dispensing 5 drops of the solution onto a holy carbon film on a Cu TEM grid, and letting dry in air before placing into the TEM. Diffraction patterns were taken by electron beam scattering diffraction to determine composition versus morphology of the nanowire. X-ray diffraction (XRD) is taken on a Scintag Diffraktometer with a Cu X-ray source at a scan rate of .02° min^{-1} scan rate at a range of 20–90° to determine the bulk composition of the sample and to verify the phase information shown in the diffraction patterns. Finally Raman spectroscopy is taken through a Horiba confocal Raman spectroscopy tool and spectroscopy is used to determine the surface phases present.

2.3. Electrochemical analysis

Cyclic voltammetry (CV) and chronopotentiometry (constant current charging/constant current discharging (CCC/CCD)) is performed on the nanowire samples using a PAR 2273 potentiostat. CV is performed in a half cell setup placed in a beaker filled with electrolyte, and CCC/CCD is performed on samples in a full cell setup placed in a pouch cell. The electrolyte used in both the full and half cell testing is a 1 M lithium hexafluorophosphate (LiPF$_6$) dissolved in a 1:1 mixture of ethylene carbonate (EC):diethyl carbonate (DEC) solution (Sigma Aldrich). CV is done in a half cell setup by draping the nanowire sample and Li wire (Sigma Aldrich) counter and reference electrode in a beaker filled with electrolyte and cycled. CCC/CCD is performed on full pouch cells comprised of sandwiched stack of an aluminum current collector coated with lithium iron phosphate (LiFePO$_4$) powder (MTI Corporation), a 20 μm thick microporous polyethylene separator (Celgard), and the nanowire sample grown directly on a stainless steel substrate. The stack is placed in a heat sealable pouch with the anode and cathode cut so that an electrical lead sticks out of the pouch. The pouch is sealed on 3 sides and then electrolyte is squirted into the pouch dousing the anode, cathode, separator and the fourth side of the pouch is sealed. The cells were fabricated and tested in a Vacuum Atmospheres argon filled glovebox with binding post electrical feedthrus to connect the potentiostats through the glovebox to the test cells. This is done to keep the cells in an inert environment during cycling.

3. Results and discussion

3.1. Material phase and morphology

The top down and cross sectional morphology results for all 3 different growth regimes are shown by TEM and SEM in Fig. 1. Shown in Fig. 1 is the diffraction pattern for all 3 different growth regimes which shows a clear single crystal diamond diffraction pattern for the samples with no catalyst as shown in Fig. 1g. The diffraction pattern for 30 nm thick Ni catalyzed nanowire pattern compliant with a multicrystalline cubic crystal lattice is shown in Fig. 1h [19]. The diffraction pattern for 70 nm thick Ni catalyzed nanowires is compliant with a multicrystalline orthorhombic pattern is shown in Fig. 1e [19]. The surface coverage of the sample as shown by the SEM micrographs is good for the 30 nm thick catalyst sample and poor for the 70 nm and no catalyst layer samples as shown in Fig. 1b–d. For no catalyst layer the SiNW are

catalyzed by Fe from the stainless steel current collector or other contaminants [8,18,20]. The high alloying temperature of Fe would make metal induced growth unfavorable creating pure SiNW growth as can be seen from the diamond lattice diffraction pattern by the TEM micrograph in Fig. 1g [1–5] The growth of the 70 nm Ni catalyst layer would be common to Ni catalyzed metal induced growth as shown in literature [16,17]. The poor surface coverage is attributable to the tendency for Ni to agglomerate in thicker layers when heated [16,17]. The TEM diffraction pattern shows a diffraction pattern compliant with a multicrystalline orthorhombic crystal lattice of NiSi and the TEM micrograph the contrast between different crystal orientations is apparent as shown in Fig. 1f and i [19]. For the 30 nm Ni catalyst layer a novel interaction occurs since at thinner layers Ni is less likely to agglomerate up and the catalyst layer is exhausted during the growth with the continued decomposition of Si from SiH_4 onto the sidewalls of the nanowires [16,17]. This provides a nanowire layer that has good surface coverage and
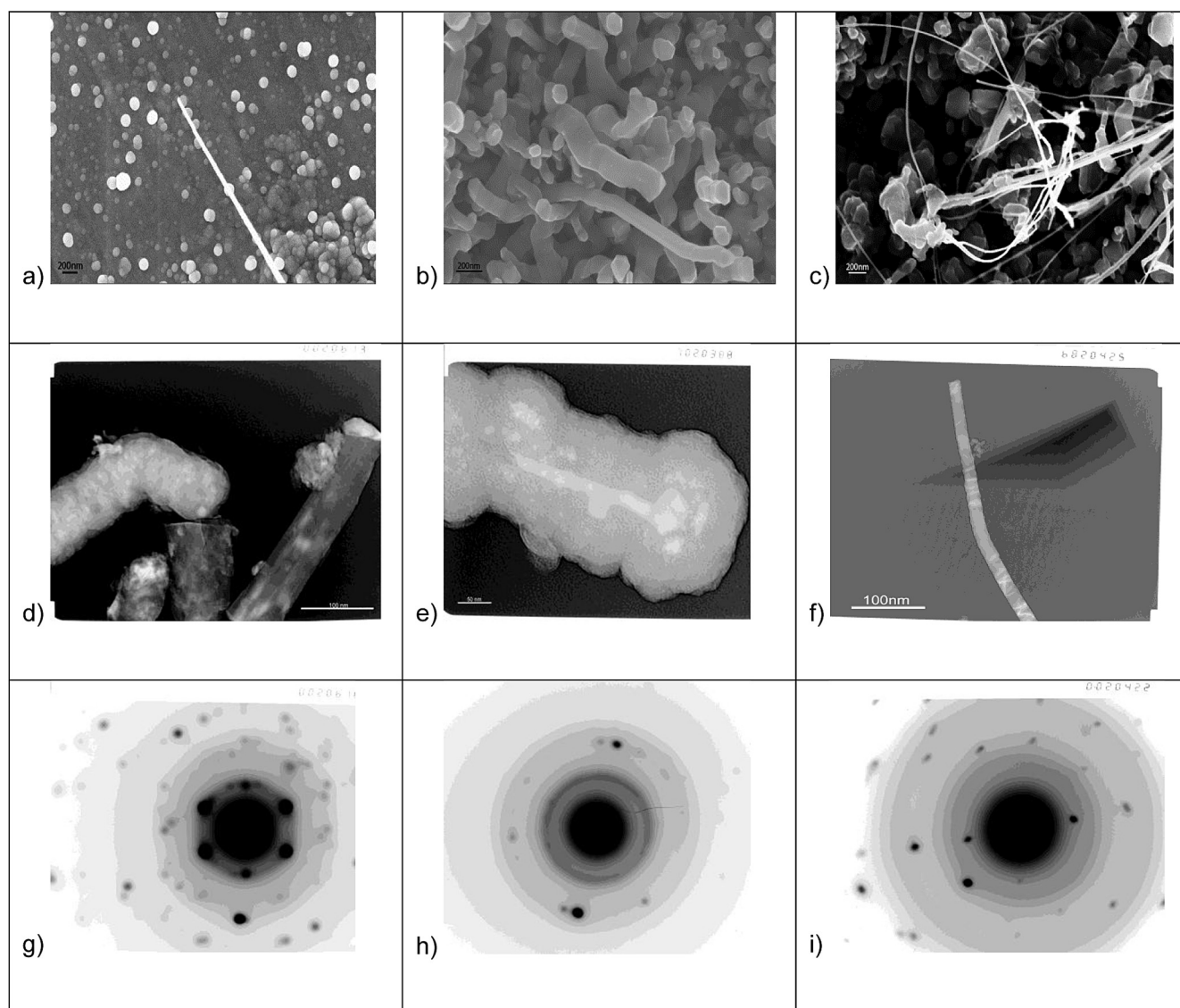

Fig. 1. Images of SiNW grown with different catalyst layer thicknesses on a 304 stainless steel substrate. For the TEM micrographs the substrates are sonicated in an ethyl alcohol bath. 5 drops of the sonicated liquid is taken in an eyedropper and placed on a Cu TEM grid with a carbon film on it. Figure a) SEM of nanowires with no catalyst layer, b) SEM of nanowires with 30 nm Ni catalyst layer, c) SEM of nanowires with 70 nm Ni catalyst layer, d) TEM of nanowires with no catalyst layer, e) TEM of nanowires with 30 nm Ni catalyst layer, f) TEM of nanowires with 70 nm Ni catalyst layer, g) TEM diffraction pattern of nanowires with no catalyst layer showing diamond diffraction pattern, h) TEM of nanowires with 30 nm Ni catalyst layer showing a multicrystalline diffraction pattern indexed to be a cubic crystal lattice, i) TEM diffraction pattern of nanowires with 70 nm Ni catalyst layer catalyst layer showing a multicrystalline diffraction pattern indexed to be a body centered orthorhombic crystal lattice.

heterogeneous nanowire morphology. From the SEM micrographs it is observed that the nanowires are shorter and fatter than the thicker catalyst layer samples which would be compliant with the exhaustion of the catalyst particles during metal induced growth followed by continued Si deposition by SiH_4 thermal decomposition. The heterogeneous morphology as witnessed in the TEM micrograph Fig. 1e solidifies this premise. For the 30 nm Ni catalyzed nanowire samples the inside core shows a TEM diffraction pattern that is compliant with a multicrystalline cubic crystal lattice which would imply that the inside core is in the nickel disilicide phase $NiSi_2$ [19]. To check the phases present in each grown nanowire system XRD and Raman are performed on the samples.

The results of Raman and XRD are shown for all samples along with the spectrum for a blank stainless steel current collector and a stainless steel current collector with 70 nm of Ni deposited on top are shown in Fig. 2a for the XRD response, and Fig. 2b for the Raman response [21–27]. The XRD response for plain stainless steel substrate shows 3 characteristic austenitic steel peaks. The Ni coated sample also shows the same 3 peaks due to the overlap of the Ni (200) peak and the austenitic steel (200) peak, also because austenitic steel contains up to 11% Ni. The nanowires grown with no catalyst show a small Si peak at 38° which is compliant with the as observed single crystalline SiNW [21–26]. The Raman spectrum also shows a characteristic Si peak at 520 cm^{-1} with no other peaks present [24–26]. For the 70 nm Ni catalyzed nanowires the XRD

Fig. 2. XRD and Raman spectroscopy of different stages during sample deposition with the different stages plotted on the same graph with an offset of amplitude applied to each spectrum profile in order to see all of them. The peaks are labeled with the XRD spectrum shown in Figure a) and the Raman spectrum shown in Figure b).

spectrum shows a characteristic NiSi peak at 47° and the Raman Spectrum shows a double peak around 200 cm^{-1} which is compliant with characteristic peaks for NiSi at 196 and 213 cm^{-1} [21–27]. The 30 nm thick catalyst layer shows an XRD peak around 28 and 47° for $NiSi_2$ which is compliant with the TEM diffraction patterns [21–26]. The Raman spectrum shows a peak centered around 371 cm^{-1} which is characteristic to $NiSi_2$ and a wide Si peak at 500 cm^{-1} which is compliant with amorphous Si (a-Si) peak at 480 cm^{-1} and a crystalline Si peak at 520 cm^{-1} [24–26]. The difference phases between the growth kinetics to produce the two different phases of silicide in the 30 nm and 70 nm catalyzed samples were not expected. It has been shown that $NiSi_2$ has been grown under the formation temperature in nanostructures due to high Gibb's free energy surfaces, but the results show that the nanowire samples with no surface coating retains the NiSi phase while the nanowire samples with a surface coating obtain a Ni poor silicide phase which implies that the excess Ni continues to diffuse into the a-Si shell. To better understand the composition of the outside amorphous region the 30 nm Ni catalyzed nanowire sample was investigated by energy electron loss spectroscopy (EELS) in a high resolution JEOL 1550 TEM.

The results of the EELS analysis is shown in Fig. 3 with the separate images mapped for energy spectrum associated with each material. The material mapping for Si is shown in Fig. 3b which shows that there is Si within the crystalline core which is compliant with the $NiSi_2$ phase and in the outside shell which is compliant with the proposed process step that the a-Si deposition occurs when the Ni catalyst is exhausted. The mapping for Fe shown in Fig. 3c shows a negligible Fe signal which is checked just in case of Fe contamination occurs from the current collector as an unsuspected interaction. The mapping for C is shown in Fig. 3d also showing a negligible signal and is probed for contamination purposes. The mapping for O is shown in Fig. 3e and in the O spectrum significant signal is shown on the interface which is expected for surface passivation but also throughout the whole amorphous structure. The incorporation of O into the amorphous shell region can be explained by the oxygen gettering of a-Si as seen in multiple solid liquid solid (SLS) silicon nanowire growth papers, and also by the possible incorporation of H which also has oxygen gettering qualities when bonded with Si [28,29]. The Ni mapping is shown in Fig. 3f with a large signal shown in the crystalline core of the nanowire which is compliant with having a multicrystalline $NiSi_2$ core, but there is also a signal from the amorphous shell. The process of diffusion for Ni from the $NiSi_2$ multicrystalline core into the a-Si shell has not been observed previously. It is speculated that this diffusion occurs due to the desire for Ni to diffuse into Si at elevated temperatures and would explain the difference in silicide phases between the two nanowire systems. From phase diagrams it is observed that a phase consisting of Ni–Si–O that Ni would remain unoxidized when doped in a SiO structure [30]. However as seen in Fig. 2 there appears a signal for NiO which we attribute to Ni not only being on the core of the amorphous shell but also on the surface as well.

3.2. Electrochemical performance

Cyclic voltammetry is performed on all 3 samples for 90 cycles between 0 and 2 V at a scan rate of 1 mV s^{-1} with performance for each sample shown in Fig. 4. CV is an electrochemical method in which potential is stepped from an initial potential at a constant rate until a final potential is reached and then the potential is decreased to the initial potential at the same rate. Rises and depressions in current as measured on the CV diagram correspond to the production or the consumption of current carrying species at a specific potential. The production or consumption of the current
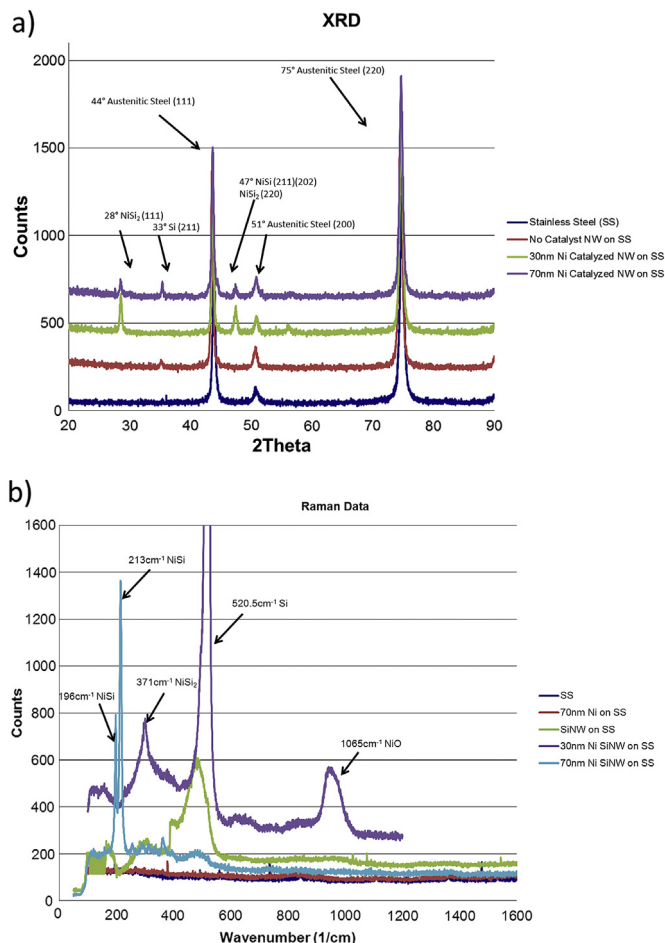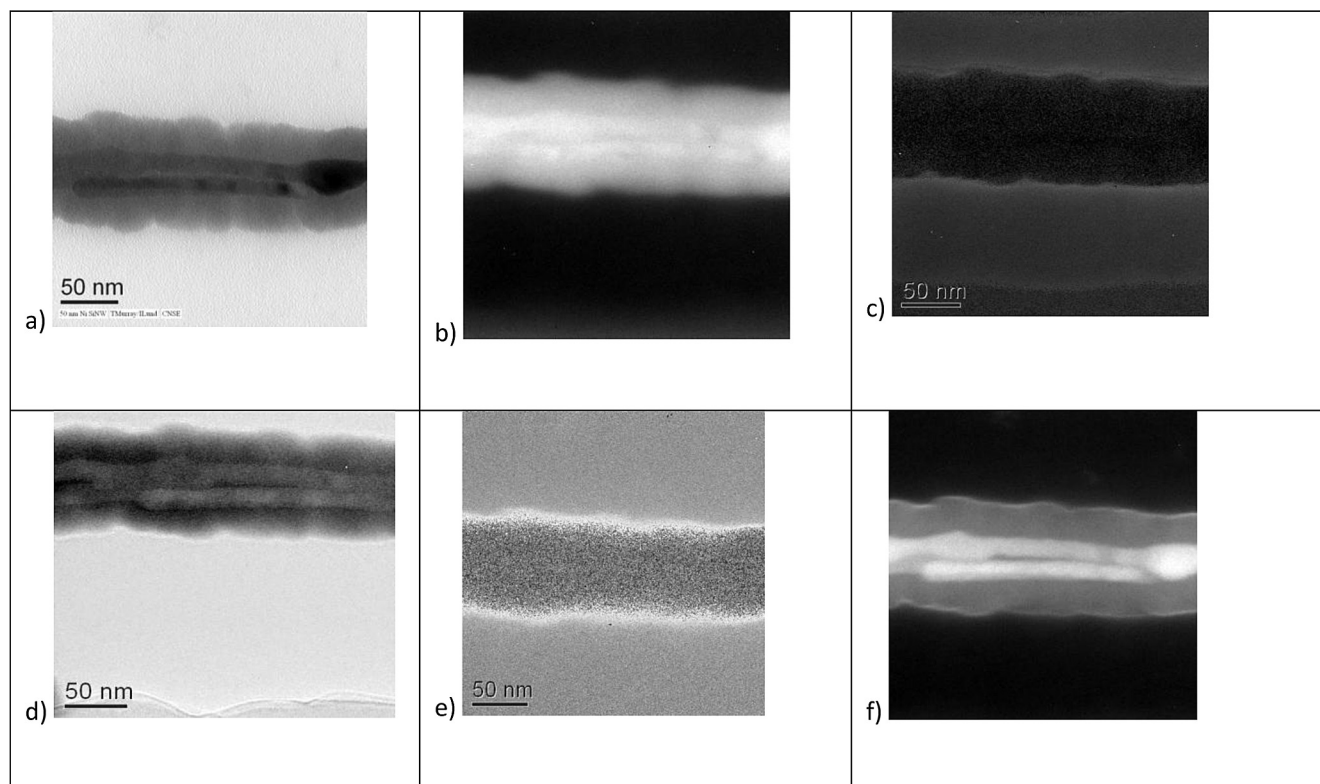
Fig. 3. a) TEM micrograph of a nanowire on a holey carbon grid, and EELS energy filtered imaging of the nanowire shown in b) Si mapping, c) Fe mapping, d) C mapping, e) O mapping, and f) Ni mapping.

carrying species at specific potentials is material dependent and leads to electro active materials characterization. CV is done over multiple cycles on each sample and the oxidation and reduction peaks are tracked to identify any material changes during cycling. A half-cell setup utilizes a three terminal setup with the nanowire sample being the working electrode and Li wire being the counter and reference electrode. The three terminal test setup allows for the isolation of internal resistance and interactions from the cathode (Li wire) from the current response of the half-cell as shown in CV. Fig. 4a shows the CV response for a half cell with the anode comprised of SiNW grown directly on a current collector without a catalyst. The CV shows the characteristic oxidation and reduction peaks for Si starting at .3 V and finishing at 0 V. There is an absence of a characteristic .5 V oxidation peak, and an appearance of a peak at .8 V that is associated with solid electrolyte interphase (SEI) formation [1–5]. In Fig. 4a it can be seen that the reduction peak associated with Si maintains the same magnitude over cycling, however the oxidation peaks shift to the right implying the consumption of Li wire to balance the Li trapping within the Si wire as proposed by Kasavajjula [8]. Fig. 4c shows the CV of the 70 nm Ni catalyzed sample. The CV shows a reduction peak that is characteristic with NiSi which separates into Ni and Si creating a drawn out reduction peak for NiSi separating and Li alloying with Si [9,14]. The oxidation starts with the same oxidation peak as for Si which would be compliant with the use of a NiSi phase as an anode material [9,14]. We can see that the peak associated with Li reduction into Si degrades to 1/3 of its original magnitude which implies that the Li performance of NiSi nanowire degrades over multiple cycles as shown previously [9,14]. Fig. 4b shows the CV for the 30 nm Ni catalyzed nanowire sample. The CV shows a reduction peak that starts at .5 V which is compliant with using SiO as an anode and the production of Li_2O [13,27,31–35]. The reduction potential increases

until 0 V as SiO decomposes into Li_2O and Si which then alloys with Li to form $Li_{4.4}Si$ [13,27,31–35]. There is also a noticeable bump within the reduction peak from .5 to 0 V at .25 V that would be attributable to the production of lithium silicates (denoted from here on as Li_xSiO_y) [13,27,31–35]. The oxidation potential stays constant at .3 V for the oxidation of Li from Si, Li from Li_xSiO_y occur at potentials starting at .39 V, a peak at .5 V for the oxidation of Li from Li_2O and an oxidation peak at .8 V which would be compliant with SEI formation [13,27,31–35]. The reduction peak height for Si at 0 V increases over cycles which would be attributable to the activation of the SiO during cycling. The formation of Li_2O and Li_xSiO_y in the lithiation of SiO as shown in Equations (2)–(4) would passivate the anode during cycling from the further formation of SEI layer formation and buffer the volume expansion of the anode by 200% [13,27,31–35]. The reversible formation of the Li_2O and Li_xSiO_y allows for a high columbic efficiency not shown previously in SiO based anode and for a higher reversible capacity attributable to the capacity holding Li_2O and Li_xSiO_y compounds [13,27,31–35]. The formation of Li_2O and Li_xSiO_y during the anode charging also would passivate the anode surface during charging and material swell thus creating a stable passivation over the full charging range. The creation of a passivation layer that swells with the anode during charging solves the unstable SEI creation problem seen in Si based anodes. Normally both the Li_2O and Li_xSiO_y are irreversible when formed during initial charging, but with the addition of a conduction pathway as seen in reaction displacement transition metal oxide anodes such as NiO or Co_3O_4, or in the doping of SiO based anodes with metallic constituents such as Ni high columbic efficiency can be achieved [33–35]. The presence of a conductive pathway can achieve good reversibility as shown by Miyachi achieving an 84% initial columbic efficiency using an 8 μm thick sheet of 25% Ni doped in SiO anode [34,35].
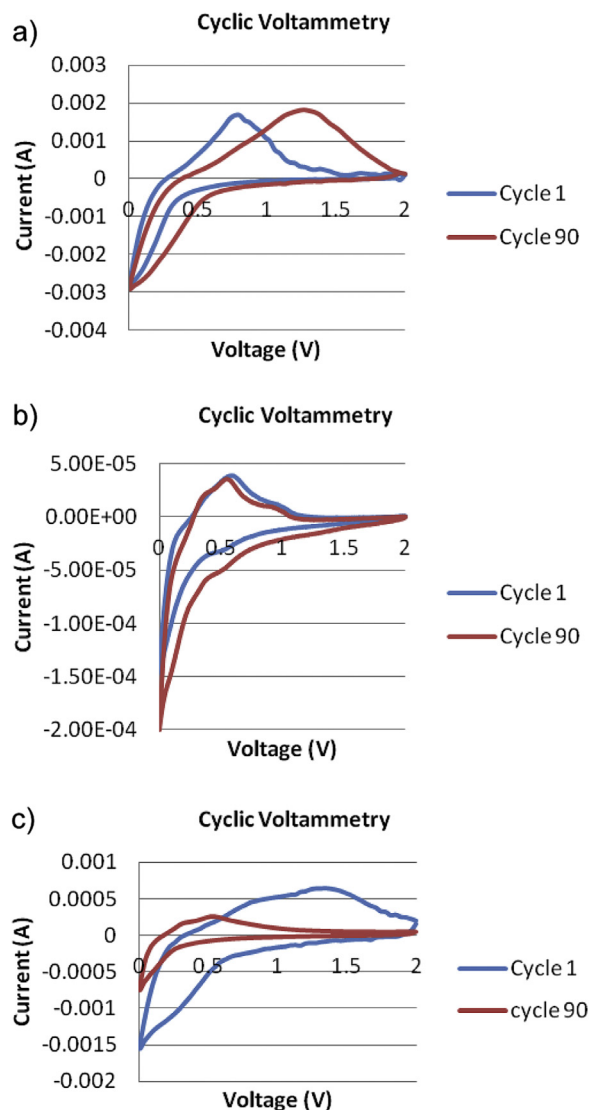
a)

b)

c)

Fig. 4. Cyclic voltammetry results for the nanowire samples cycled in a half cell for 90 cycles from 0 to 2 V with a step rate of 1 mV s^{-1} with a) CV of nanowires with no catalyst layer, b) CV of nanowires with 30 nm Ni catalyst layer, c) CV of nanowires with 70 nm Ni catalyst layer.
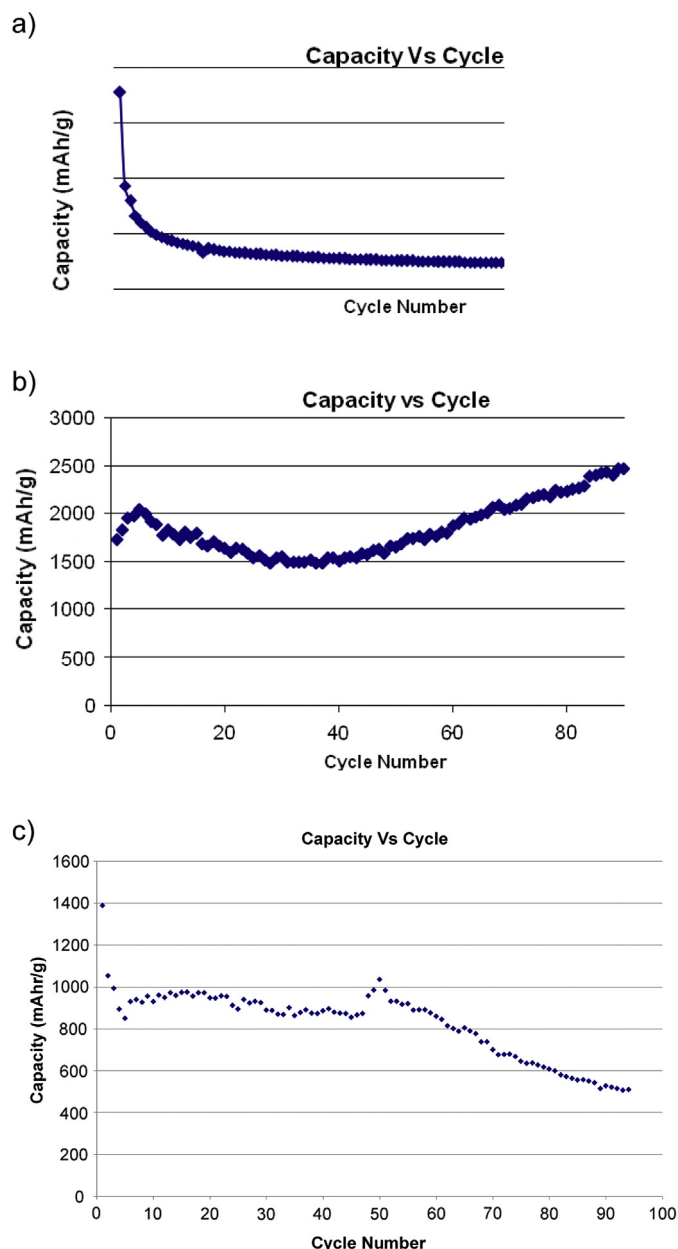
$$SiO + 2Li \leftrightarrow Li_2O + Si \tag{2}$$

$$4SiO + 4Li \leftrightarrow Li_4SiO_4 + 3Si: \text{ capacity: } 2600 \text{ mAh g}^{-1} \tag{3}$$

$$Si + 4.4Li \leftrightarrow Li_{4.4}Si \tag{4}$$

To determine the capacity and capacity retention of the anodes in a commercial geometry all three samples are subjected to CCC/CCD at a .5 C (1 charge in 2 h) rate as shown in Fig. 5. CCC/CCD is where constant current is applied for charging and discharging phase of the cell while potential is plotted over time until a cutoff potential is reached. The time it takes to charge or discharge the cell in hours times the current divided by the active material weight gives the charging and discharging capacity of the limiting electrode material (in our case the anode material). This is an industry standard test and helps determine charge rate dependent capacity if done at multiple charge rates. Fig. 5a shows the performance for the SiNW grown directly onto a current collector. The theoretical capacity of the pure SiNW is 4214 mAh g^{-1} and from the first

a)

b)

c)

Fig. 5. Chronopotentiometry results for the nanowire samples cycled at a .5 C charge rate until the charge capacity reaches 80% of its initial capacity a) CCC/CCD of nanowires with no catalyst layer, b) CCC/CCD of nanowires with 30 nm Ni catalyst layer, c) CCC/CCD of nanowires with 70 nm Ni catalyst layer.

discharge capacity of 3300 mAh g^{-1} is observed [1–5]. The pure SiNW samples capacity fell to 200 mAh g^{-1} within 10 cycles with the capacity remaining at 200 mAh g^{-1} for all cycles afterward showing poor performance caused either by Li trapping as shown in the CV diagram or by unmitigated SEI production as proposed in previous literature [1–8]. The 70 nm Ni catalyzed nanowire samples have the theoretical capacity of NiSi 1360 mAh g^{-1} with the cycling results shown in Fig. 5b [8–12,14]. The first charging capacity shows a capacity of 1390 mAh g^{-1} that steadily degrades to a capacity of 520 mAh g^{-1} after 90 cycles which would be attributable to unmitigated production of SEI. Li trapping for NiSi should not occur since the addition of Ni to the structure would assist with the conduction of electrons in the oxidation of Li from the Si structure [8]. The theoretical capacity of

the 30 nm Ni catalyzed nanowires is the combination of the theoretical capacity of SiO at 2600 mAh g^{-1} and Si at 4214 mAh g^{-1} in the amorphous shell with a decreased theoretical capacity due to the Ni doping combined with the theoretical capacity of NiSi$_2$ 562 mAh g^{-1} [13,15,27,31–35]. The experimental results are shown in Fig. 5c which shows an initial capacity of 1727 mAh g^{-1} with a capacity retention that grows during cycling to a capacity of 2468 mAh g^{-1} which is compliant with the peaks growing during the CV diagram, and would be attributable to the creation of a less dense structure during cycling which would expose more active material for charging. This occurs due to the incomplete contraction of the structure after the swelling occurring during Li$_2$O and Li$_x$SiO$_y$ formation which pushes active material apart and creates a more open structure to allow for quicker diffusion. We also attribute the reversible production of Li$_2$O and Li$_x$SiO$_y$ to the Ni doping in the amorphous shell and the thickness of the amorphous shell only being around 20–25 nm which allows for intimate contact with the highly conductive NiSi$_2$ crystalline core allowing for a good electrical pathway to assist with Li$_2$O and Li$_x$SiO$_y$ species reduction and allows for good columbic efficiency.

4. Conclusions

It is shown that the thickness of the catalyst layer thickness plays a significant role in the growth and morphology of the nanowires and its correlation to device performance when utilized as an anode material for Li-ion batteries. We present a new method of producing a heterogenous nanowire through an extinguishing of a Ni catalyst layer during a metal induced growth process which produces a nanowire with superior capacity and capacity retention when compared with other nanowire solutions. The heterogenous nanowire system shows an initial capacity of 1727 mAh g^{-1} (5× that of C) with capacity that grows to a capacity 2468 mAh g^{-1} after 90 cycles, while for a pure NiSi nanowires and pure Si nanowires the capacity falls below 45% of the initial capacity within 90 cycles. The cycling performance of the heterogenous nanowires can be attributed to the nature of the interaction of Li with SiO creating a Li$_2$O and lithium silicate passivating layer that protects the nanowire from unmitigated SEI growth and capacity degradation over multiple charging and discharging cycles.

Acknowledgments

References

[1] C.K. Chan, R. Ruffo, S.S. Hong, Y. Cui, J. Power Sources 189 (2009) 1132–1140.
[2] M.H. Park, M.G. Kim, J. Joo, K. Kim, J. Kim, S. Ahn, J. Cho, Nano Lett. 9 (11) (2009) 3844–3847.
[3] Z. Zhou, Y. Xu, W. Liu, L. Niu, J. Alloys Compd. 493 (2010) 636–639.
[4] L.F. Cui, R. Ruffo, C.K. Chan, H. Peng, Y. Cui, Nano Lett. 9 (1) (2009) 491–495.
[5] Y.M. Lee, J.Y. Lee, H.T. Shim, J.K. Lee, J.K. Park, J. Electrochem. Soc. 154 (6) (2007) A515–A519.
[6] X.H. Liu, L. Zhong, S. Huang, S.X. Mao, T. Zhu, J.Y. Huang, ACS Nano 6 (2) (2012) 1522–1531.
[7] W. Xu, Master's thesis, B.S. Dalian University of Technology, Lousiana State University, August 2011.
[8] U. Kasavajjula, C. Wang, A.J. Appleby, J. Power Sources 163 (2007) 1003–1039.
[9] W.-R. Liu, N.-L. Wu, D.-T. Shieh, H.-C. Wu, M.-H. Yang, C. Korepp, J.O. Besenhard, M. Winter, J. Electrochem. Soc. 154 (2) (2007) A97–A102.
[10] H.-L. Zhang, F. Li, C. Liu, H.-M. Cheng, Nanotechnology 19 (2008) 165606, 7pp.
[11] M.-S. Park, Y.-J. Lee, S. Rajendran, M.-S. Song, H.-S. Kim, J.-Y. Lee, Electrochim. Acta 50 (2005) 5561–5567.
[12] H.-Y. Lee, Y.-L. Kim, M.-K. Hong, S.-M. Lee, J. Power Sources 141 (2005) 159–162.
[13] G.X. Wang, L. Sun, D.H. Bradhurst, S. Zhong, S.X. Dou, H.K. Liu, J. Power Sources 88 (2000) 278–281.
[14] G.X. Wang, L. Sun, D.H. Bradhurst, S. Zhong, S.X. Dou, H.K. Liu, J. Alloys Compd. 306 (2000) 249–252.
[15] T. Kim, S. Park, S.M. Oh, Electrochem. Commun. 8 (2006) 1461–1467.
[16] C.-J. Kim, K. Kang, Y.S. Woo, K.-G. Ryu, H. Moon, J.-M. Kim, D.-S. Zang, M.-H. Jo, Adv. Mater. 19 (21) (November, 2007) 3637–3642.
[17] J. Kim, W.A. Anderson, Thin Solid Films 483 (2005) 60–65.
[18] V. Schmidt, J.V. Wittemann, U. Gosele, Chem. Rev. 110 (2010) 361–388.
[19] T. Shiozawa, Master Thesis, Iwai Laboratory Department of Electronics and Applied Physics, Tokyo Institute of Technology.
[20] G. Zhou, J.C. Yang, F. Xu, J.A. Barnard, Mater. Res. Soc. Symp. Proc. 737 (2003).
[21] W.-S. Lee, T.-H. Chen, C.-F. Lin, J.-M. Chen, Appl. Phys. A 100 (2010) 1089–1096.
[22] S.Y. Tan, C.-W. Chen, I.-T. Chen, C.-W. Feng, Thin Solid Films 517 (2008) 1186–1190.
[23] X. Guo, H. Yu, Y.-L. Jiang, G.-P. Ru, D.W. Zhang, B.-Z. Li, Appl. Surf. Sci. 257 (2011) 10571–10575.
[24] Y.-L. Jiang, A. Agarwal, G.-P. Ru, G. Cai, B.-Z. Li, Nucl. Instrum. Meth. Phys. Res. B 237 (2005) 160–166.
[25] L. Wan, X. Zhang, B. Tang, Y. Ren, X. Cheng, D. Xu, H. Luo, Y. Huang, Thin Solid Films 518 (2010) 3646–3649.
[26] F.F. Zhao, J.Z. Zheng, Z.X. Shen, T. Osipowicz, W.Z. Gao, L.H. Chan, Microelectron. Eng. 71 (2004) 104–111.
[27] C.-H. Doh, C.-W. Park, H.-M. Shin, D.-H. Kim, Y.-D. Chung, S.-I. Moon, B.-S. Jin, H.-S. Kim, A. Veluchamy, J. Power Sources 179 (2008) 367–370.
[28] X. Ou, R. Kogler, A. Mucklich, W. Skorupa, W. Moller, X. Wang, J.W. Gurlach, B. Rauschenbach, Appl. Phys. Lett. 93 (2008) 161907.
[29] D. Maroudas, R.A. Brown, Appl. Phys. Lett. 58 (17) (1991).
[30] P.S. Lee, D. Magnelinck, K.L. Pey, J. Ding, J.Y. Dai, C.S. Ho, A. See, Microelectron. Eng. 51–52 (2000) 583–594.
[31] C. Guo, D. Wang, Q. Wang, B. Wang, T. Liu, Int. J. Electrochem. Sci. 7 (2012) 8745–8752.
[32] M. Miyachi, H. Yamamoto, H. Kawai, T. Ohta, M. Shirakata, J. Electrochem. Soc. 152 (10) (2005) A2089–A2091.
[33] Y.-M. Kang, K.-T. Kim, J.-H. Kim, H.-S. Kim, P.S. Lee, J.-Y. Lee, H.K. Liu, S.X. Duo, J. Power Sources 133 (2004) 252–259.
[34] W.-S. Chang, C.-M. Park, J.-H. Kim, Y.-U. Kim, G. Jeong, H.-J. Sohn, Energy Environ. Sci. 5 (2012) 6895.
[35] M. Miyachi, H. Yamamoto, H. Kawai, J. Electrochem. Soc. 154 (4) (2007) A376–A380.